

# Large anomalous Hall current induced by topological nodal lines in a ferromagnetic van der Waals semimetal

Kyoo Kim<sup>1,2,10</sup>, Junho Seo<sup>1,3,10</sup>, Eunwoo Lee<sup>4,5,6</sup>, K.-T. Ko<sup>1,2</sup>, B. S. Kim<sup>4,5</sup>, Bo Gyu Jang<sup>7</sup>, Jong Mok Ok<sup>1,3</sup>, Jinwon Lee<sup>1,3</sup>, Youn Jung Jo<sup>8</sup>, Woun Kang<sup>10</sup>, Ji Hoon Shim<sup>7</sup>, C. Kim<sup>4,5</sup>, Han Woong Yeom<sup>1,3</sup>, Byung Il Min<sup>1</sup>, Bohm-Jung Yang<sup>4,5,6\*</sup> and Jun Sung Kim<sup>1,3\*</sup>

**Topological semimetals host electronic structures with several band-contact points or lines and are generally expected to exhibit strong topological responses. Up to now, most work has been limited to non-magnetic materials and the interplay between topology and magnetism in this class of quantum materials has been largely unexplored. Here we utilize theoretical calculations, magnetotransport and angle-resolved photoemission spectroscopy to propose  $\text{Fe}_3\text{GeTe}_2$ , a van der Waals material, as a candidate ferromagnetic (FM) nodal line semimetal. We find that the spin degree of freedom is fully quenched by the large FM polarization, but the line degeneracy is protected by crystalline symmetries that connect two orbitals in adjacent layers. This orbital-driven nodal line is tunable by spin orientation due to spin-orbit coupling and produces a large Berry curvature, which leads to a large anomalous Hall current, angle and factor. These results demonstrate that FM topological semimetals hold significant potential for spin- and orbital-dependent electronic functionalities.**

The interplay of symmetry and topology is important not only to determine the bulk topological invariant of an insulator, but also to characterize the nodal points or nodal lines of a topological semimetal<sup>1,2</sup>. Depending on the node degeneracy and its dimension, different types of topological semimetals have been proposed theoretically<sup>3–11</sup>, such as Dirac-, Weyl-, double Dirac- and nodal-line semimetals, some of which are confirmed experimentally<sup>12,13</sup> and exhibit unusual physical properties<sup>14–16</sup>. Even more exotic properties are expected if a topological semimetal is realized in a ferromagnetic (FM) system with broken time reversal ( $T$ ) symmetry<sup>17,18</sup>. These include the enhanced anomalous Hall effect (AHE)<sup>19</sup>, magnetically tunable point nodes<sup>18</sup>, and emergent domain wall properties<sup>20</sup>, which are potentially important for spin-related electronic applications. Despite these interesting theoretical proposals, the discovery of FM topological semimetals, especially those with line nodes near the Fermi level ( $E_F$ ), have remained elusive because of the lack of suitable materials. In this work, we show that a magnetic van der Waals (vdW) material,  $\text{Fe}_3\text{GeTe}_2$ , is a candidate FM nodal-line semimetal.

$\text{Fe}_3\text{GeTe}_2$  is a rare example of itinerant vdW ferromagnets with a high Curie temperature of  $T_c = 220\text{ K}$  (refs. <sup>21,22</sup>). It has a layered hexagonal crystal structure in which  $\text{Fe}_3\text{Ge}$  slabs, sandwiched by Te layers, are coupled via vdW interaction (Fig. 1a). There are two inequivalent Fe atomic sites, denoted as  $\text{Fe}^{\text{I}}$  and  $\text{Fe}^{\text{II}}$ , respectively. The  $\text{Fe}^{\text{I}}-\text{Fe}^{\text{I}}$  dumbbells are located at the centre of every hexagonal plaquettes in the honeycomb lattice, composed of covalently bonded  $\text{Fe}^{\text{II}}$  and Ge atoms (Fig. 1b). The staking of these  $\text{Fe}^{\text{II}}$ -Ge honeycomb

lattices in the so-called AB bilayer configuration (Fig. 1c) determines the overall crystalline symmetry of the system. In ferromagnets with the fully quenched spin degree of freedom, the crystalline symmetry is important to induce the band degeneracy between the Bloch states that carry different orbital angular momenta, as discussed below.

To understand the effect of the crystalline symmetry on the topological band structures, we first describe the symmetry of a bilayer structure. The symmetry of an  $\text{Fe}^{\text{II}}\text{Ge}$  bilayer (Fig. 1c) belongs to the space group  $P\bar{3}1m$  (No. 164) that is generated by a three-fold rotation about the  $z$  axis ( $C_{3z}$ ), a two-fold rotation about the  $y$  axis ( $C_{2y}$ ) and an inversion ( $P$ ). At the K point in the Brillouin zone (BZ), the system is invariant under  $C_{3z}$ ,  $C_{2y}$  and  $PT$ , which allows two-dimensional (2D) irreducible symmetry representations and results in a two-fold degeneracy in the absence of spin-orbit coupling (SOC). Without SOC, spin-polarized bands can be considered as time-reversal invariant spinless states, and the remaining orbital degree of freedom is responsible for the observed two-fold degeneracy (Fig. 1e,f). This symmetry property contrasts the case of a hypothetical bilayer with the AA-type stacking (Fig. 1g). In this case, the  $C_{2y}$  and  $P$  symmetries are explicitly broken, and another two-fold rotation about the  $x$  axis ( $C_{2x}$ ) is not a relevant symmetry at the K point. Thus, the states at the K point have only one-dimensional (1D) irreducible representations labelled by the  $C_{3z}$  eigenvalues without degeneracy.

Now let us consider the bulk system  $\text{Fe}_3\text{GeTe}_2$ , which belongs to the space group  $P6_3/mmc$  (No. 194) with the symmetry generators

<sup>1</sup>Department of Physics, Pohang University of Science and Technology, Pohang, Republic of Korea. <sup>2</sup>Max Planck POSTECH/Hsinchu Center for Complex Phase Materials, Pohang University of Science and Technology, Pohang, Republic of Korea. <sup>3</sup>Center for Artificial Low Dimensional Electronic Systems, Institute for Basic Science (IBS), Pohang, Republic of Korea. <sup>4</sup>Department of Physics and Astronomy, Seoul National University, Seoul, Republic of Korea.

<sup>5</sup>Center for Correlated Electron Systems, Institute for Basic Science (IBS), Seoul, Republic of Korea. <sup>6</sup>Center for Theoretical Physics (CTP), Seoul National University, Seoul, Republic of Korea. <sup>7</sup>Department of Chemistry, Pohang University of Science and Technology, Pohang, Republic of Korea. <sup>8</sup>Department of Physics, Kyungpook National University, Daegu, Republic of Korea. <sup>9</sup>Department of Physics, Ewha Womans University, Seoul, Republic of Korea.

<sup>10</sup>These authors contributed equally: Kyoo Kim, Junho Seo. \*e-mail: [bjyang@snu.ac.kr](mailto:bjyang@snu.ac.kr); [js.kim@postech.ac.kr](mailto:js.kim@postech.ac.kr)

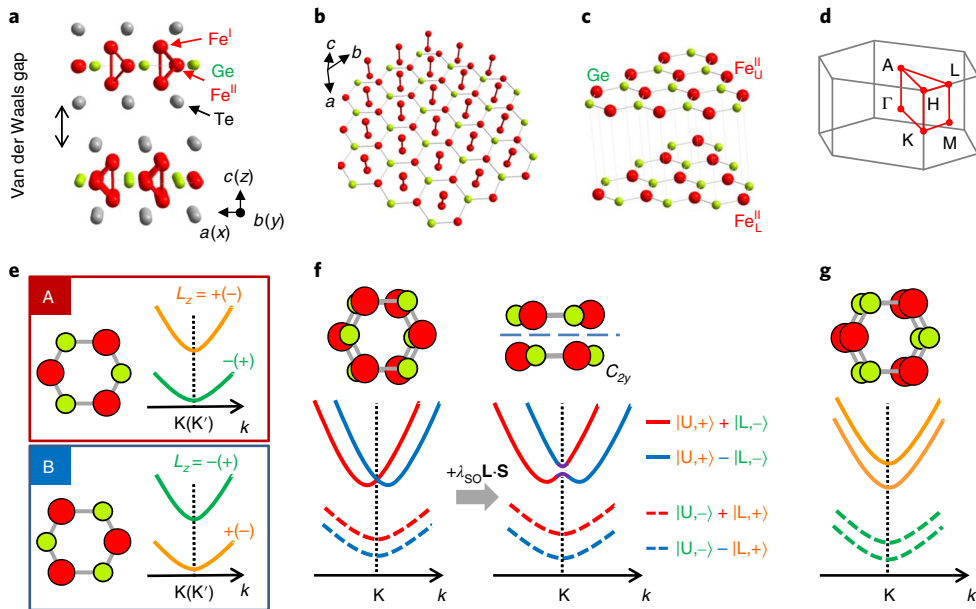


**Fig. 1 | Lattice structure of  $\text{Fe}_3\text{GeTe}_2$  and the mechanism for the two-fold degeneracy at the K and  $\text{K}'$  points in the BZ.** **a**, Structure of a  $\text{Fe}_3\text{GeTe}_2$  bilayer. **b**, Structure of a  $\text{Fe}_3\text{Ge}$  monolayer. **c**, Simplified structures for a  $\text{Fe}_3\text{GeTe}_2$  bilayer in which only the  $\text{Fe}^{\text{II}}$  and Ge atoms are drawn. **d**, BZ of  $\text{Fe}_3\text{GeTe}_2$  with the high symmetry points and lines indicated. **e**, Orbital splitting of eigenstates at the K ( $\text{K}'$ ) points for each layer with different atomic configurations, the A and B types. The orbital angular momentum  $L_z$  at the K ( $\text{K}'$ ) point is opposite in sign between the A- and B-type layers. **f**, The band structure at the K point including interlayer hybridization for an AB stacked bilayer. The orbital-driven band degeneracy occurs at the K ( $\text{K}'$ ) point, protected by a two-fold rotation about the y axis,  $C_{2y}$ . This can be lifted by the  $\lambda_{\text{SO}}\mathbf{L}\cdot\mathbf{S}$  (see text). The orbital degrees of freedom are indicated by  $\pm$ , and layer one is denoted by U or L. **g**, The band structure for an AA stacked bilayer.

$\tilde{C}_{6z} = \left\{ C_{6z} \mid \frac{1}{2}\hat{z} \right\}$ ,  $C_{2y}$  and  $P$ . At the K (and H) point in the BZ, the system is invariant under  $\tilde{C}_{6z}P$ ,  $C_{2y}$  and  $PT$ , which allows 2D irreducible representations for the same symmetry reason as in the AB bilayer structure. The band structure calculations confirm that, in the absence of SOC, two orthogonal bands cross at the K point near  $E_F$  (Fig. 2a) and resemble the typical Mexican-hat shaped bands induced by the Rashba effect (Fig. 2b). However, unlike the conventional Rashba systems with Kramers degeneracy, here the spin degree of freedom is fully quenched and cannot construct the spinor state relevant to the crossed bands. A detailed analysis identifies that the orbital character of these crossing bands is mostly a mixture of  $3d$  orbitals with angular momenta  $L_z = \pm 1$  and  $\pm 2$  from the  $\text{Fe}^{\text{I}}-\text{Fe}^{\text{I}}$  dumbbells and  $\text{Fe}^{\text{II}}$  sites, respectively. The two orthogonal eigenstates that cross at the K point are given by  $\psi_{1,k} = |L_z = +1\rangle_L^I + |L_z = +2\rangle_L^{II}$  and  $\psi_{2,k} = |L_z = -1\rangle_U^I + |L_z = -2\rangle_U^{II}$ , where  $|L_z = \pm 1\rangle^I$  is an anti bonding state of a  $\text{Fe}^{\text{I}}-\text{Fe}^{\text{I}}$  dumbbell,  $|L_z = \pm 2\rangle^{II}$  is the state of a  $\text{Fe}^{\text{II}}$  site and the layer degree of freedom is denoted as U (L) for the upper (lower) layer (Fig. 1e). The resulting state near the K point is then described by  $\psi_k = \frac{1}{\sqrt{2}}(\psi_{1,k} + e^{i\phi_k}\psi_{2,k})$ , where  $\phi_k$  corresponds to the relative amplitude of the wavefunctions with opposite orbital and layer degrees of freedom, related by  $C_{2y}$  or  $PT$  (Fig. 1f). Taking  $\psi_{1,k}$  and  $\psi_{2,k}$  as the bases for the symmetry representation around the K point, the two symmetry generators  $\tilde{C}_{6z}P$  and  $C_{2y}$  are represented by  $\tilde{C}_{6z}P = \cos\frac{2\pi}{3} + i\sin\frac{2\pi}{3}\tau_z$  and  $C_{2y} = \tau_x$ , respectively, where  $\tau_{x,y,z}$  are the Pauli matrices in the representation of the two states  $\psi_{1,k}$  and  $\psi_{2,k}$ . It is straightforward to show that the effective Hamiltonian is given by:

$$H_0 = \epsilon_0 + \frac{1}{2m_{xy}}(k_x^2 + k_y^2) + \frac{1}{2m_z}k_z^2 + \alpha [k_y\tau_x + k_x\tau_y] \quad (1)$$

where  $\epsilon_0 = -0.03 \text{ eV}$ ,  $m_{xy} = 0.077 \text{ eV}^{-1}\text{\AA}^{-2}$ ,  $m_z = 0.036 \text{ eV}^{-1}\text{\AA}^{-2}$  and  $\alpha = 0.71 \text{ eV\AA}$  are constants with the setting  $\hbar = 1$ , estimated from

band calculations, and the momentum  $\mathbf{k}$  is measured relative to the K point. This clearly reveals the band crossing with the Dresselhaus-type orbital texture around the K point.

More interestingly, the region in which the two-fold degenerate state appears is not limited to near the K point, but extends along the KH line in the BZ (Fig. 1d). In the absence of SOC, the characteristic band crossings in every 2D plane with different  $k_z$  along the KH line (Fig. 2a and Supplementary Note 1) are described by the same effective Dresselhaus Hamiltonian in equation (1). Thus, two nodal lines, one along the KH line and the other along the  $\text{K}'\text{H}'$  line, run across the BZ, and their two-fold degeneracy is protected by  $C_{3z}$  and  $\tilde{C}_{6z}M_y$  (or  $PT$ ) symmetries. The role of the  $\tilde{C}_{6z}M_y$  symmetry at the nodal line is same as that of  $C_{2y}$  at the K point, although the nature of the related orbitals is different, as discussed in Methods. We also confirm that such a nodal-line structure is robust against electron correlation and disorder, as long as the relevant symmetries are preserved on average (Supplementary Note 2).

With the presence of nodal lines in  $\text{Fe}_3\text{GeTe}_2$  established, we now discuss the influence of SOC. In general, the SOC has the form  $H_{\text{SO}} = \lambda_{\text{SO}}\mathbf{L}\cdot\mathbf{S}$ , where  $\lambda_{\text{SO}}$  is the strength of the SOC, and  $\mathbf{L}$  and  $\mathbf{S}$  are the orbital and spin angular momenta, respectively. In a ferromagnet with  $\langle \mathbf{S} \rangle \neq 0$ , the SOC term can be treated as  $H_{\text{SO}} \approx \lambda_{\text{SO}}\mathbf{L}\cdot\langle \mathbf{S} \rangle$ , and thus it works as an orbital analogue of the Zeeman energy term. In the 2D manifold spanned by  $\psi_{1,k}$  and  $\psi_{2,k}$ , one can find that  $\langle L_x \rangle = \langle L_y \rangle = 0$  and  $\langle L_z \rangle = \frac{4}{3}\tau_z$ . Therefore, the SOC lifts the two-fold degeneracy along the nodal line only for  $\mathbf{S} \parallel z$ . The band structure calculations with SOC show that the band crossing remains intact with  $\mathbf{S} \parallel x$  (or  $y$ ), whereas a SOC gap of  $\sim 60 \text{ meV}$  opens along the nodal line for  $\mathbf{S} \parallel z$ . Depending on the canting angle of  $\mathbf{S}$  with respect to the  $z$  direction, the SOC gap is modulated continuously, as shown in Supplementary Fig. 4. Thus, the stability of the nodal line and the SOC gap are tunable by the spin orientation, which highlights the unique interplay of ferromagnetism and topology in  $\text{Fe}_3\text{GeTe}_2$ .

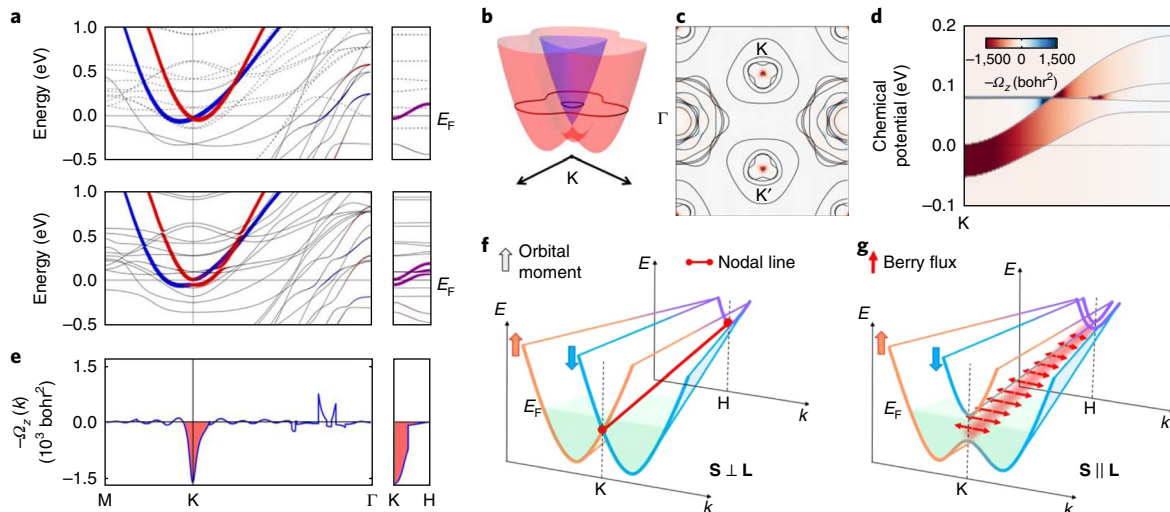


**Fig. 2 | Nodal-line band crossing and its large Berry curvature in  $\text{Fe}_3\text{GeTe}_2$ .** **a**, Calculated electronic structures of  $\text{Fe}_3\text{GeTe}_2$  without (upper panel) and with (lower panel) SOC for the majority (solid) and minority (dashed) spins. The colours indicate two orthogonal states near  $E_F$  with opposite orbital and layer degrees of freedom,  $\psi_{1,k} = |L_z = +1\rangle_U^\dagger + |L_z = +2\rangle_U^\dagger$  and  $\psi_{2,k} = |L_z = -1\rangle_L^\dagger + |L_z = -2\rangle_L^\dagger$ , where  $|L_z = \pm 1\rangle$  is the antibonding state of a  $\text{Fe}^{\text{l}}-\text{Fe}^{\text{l}}$  dumbbell, and  $|L_z = \pm 2\rangle$  is the state of the  $\text{Fe}^{\text{ll}}$  site. **b**, The Mexican-hat shaped energy dispersion without SOC near the K point. **c**, FS and Berry curvature  $-\Omega_z(k)$  in the  $k_z=0$  plane. The major contribution comes from the region near the K and  $K'$  points. **d**, Berry curvature at different  $k_z$  points along the K-H symmetry line as a function of the chemical potential. The dominant contribution to the Berry curvature comes from the anticrossing point of the majority spin bands along the nodal line, with additional contributions from the nearly dispersionless minority bands, indicated by the horizontal lines located at  $\sim 80$  meV above the  $E_F$ , is also introduced. **e**, Corresponding Berry curvature along the symmetry lines. The large contribution near the K point is marked by a shaded area. **f,g**, Schematic illustration of the nodal-line structure along the K-H symmetry line for  $S \perp L$  (**f**) and  $S \parallel L$  (**g**). The opposite orbital momenta  $L$  along z are indicated by thick arrows. With the SOC gap opening, the nodal line acts as a 1D vortex line that generates Berry flux in the momentum space, as illustrated by the thinner red arrows.

In  $\text{Fe}_3\text{GeTe}_2$ , the magnetic crystalline anisotropy prefers the spin moment  $S$  along the  $c$  axis, parallel to  $z$  in our configuration, and the avoided band crossings along the nodal lines produce a large Berry curvature (Fig. 2c,e). The nodal lines, then, can be considered as 1D magnetic vortex lines, which produce a Berry flux in the momentum space (Fig. 2g) and induce a large AHE. Ideally, if the nodal line is almost dispersionless, and  $E_F$  is located in the SOC gap, that is, in the resonance condition, every bilayer of  $\text{Fe}_3\text{GeTe}_2$ , stacked along the  $z$  direction has a quantized Hall conductance  $\frac{e^2}{h}$ . Then, the total anomalous Hall conductivity becomes as large as  $\sim \frac{e^2}{ha_z}$ , where  $e$  indicates the electric charge,  $h$  is the Planck constant and  $a_z$  is the lattice spacing along the  $z$  direction. This is equivalent to the anomalous Hall conductivity of a three-dimensional (3D) quantum Hall insulator. However, in reality, the nodal lines are dispersive along the KH direction (Fig. 2a,d), and only the part of the nodal line that satisfies the resonance condition contributes to the anomalous Hall conductivity (Fig. 2d,e). Nevertheless, the 1D nodal line in  $\text{Fe}_3\text{GeTe}_2$  produces a total Berry flux and AHE much larger than those in zero-dimensional (0D) monopoles in the momentum space of other itinerant ferromagnets, for example,  $\text{SrRuO}_3$ .

Before addressing the large AHE experimentally, we verify that the calculated band structures are, indeed, realized in  $\text{Fe}_3\text{GeTe}_2$  by using angle-resolved photoemission spectroscopy (ARPES). As shown in Fig. 3a, the Fermi surface (FS) contour map clearly identifies several pockets, which include a hexagonal-shaped FS centred at  $\Gamma$  and six circular-shaped FSs at the K points. The observed FSs agree well with the calculations based on density functional theory (DFT) (Fig. 3b). We note that the minority-spin FS with a strong 2D character is more visible than the majority-spin FS with a relatively large  $k_z$  dispersion. Some majority-spin FS is still observable, particularly near the M point, where a sizable ARPES intensity, extended along the  $\Gamma$ -M symmetry line, is consistent with a tubular FS from the majority-spin FS. These agreements in shape and size of the FSs

are significant, because the correlation effect is usually not negligible in iron-based chalcogenides<sup>23</sup>.

To identify the consistency of the band topology under the correlation effect, we calculated the momentum ( $\mathbf{k}$ )- and energy ( $\omega$ )-dependent spectral function  $A(\mathbf{k},\omega)$ , using combined DFT and the dynamical mean-field theory (DMFT) (Fig. 3d). We used an averaged on-site Coulomb interaction  $U=5.0$  eV and an exchange interaction  $J=0.9$  eV, which are typical for iron chalcogenides and are found to be appropriate for  $\text{Fe}_3\text{GeTe}_2$  (ref. <sup>24</sup>). A comparison between the DFT and DMFT bands (Fig. 3c,d) reveals that the DMFT bands are reproduced well by the renormalized DFT bands with a factor of  $\sim 1.54$ , which indicates a moderate correlation effect in  $\text{Fe}_3\text{GeTe}_2$ . In the DMFT spectra, the strong spectral damping due to the correlation effect is observed in the bands near the binding energy  $E_B=0.4-0.6$  eV, whereas the low-energy bands near  $E_B$ , particularly the band that crosses at the K points, are almost identical to the DFT bands. These features of the DMFT spectra match well with the ARPES spectra, taken along the several momentum cuts, that is, K-K, K- $\Gamma$ -K and K-M-K symmetry lines. As shown in Fig. 3e-g, the  $k_z$ -integrated DMFT spectral functions highlight several key features, such as the electron bands at the K points, the strongly dispersing bands along the  $\Gamma$ -K line and the weakly dispersing and strongly damped bands near  $E_B \approx 0.5$  eV across the whole BZ, which are clearly observed in experiments. Although the avoided band crossing at K is not clearly resolved in the ARPES spectra, due to the relatively large  $k_z$  dispersion, the overall good agreement between experiment and theory confirms that the electronic structure of  $\text{Fe}_3\text{GeTe}_2$  is explained well by DMFT as well as by DFT with a moderate renormalization. This allows us to obtain the Berry curvature and the corresponding AHE from the calculated electronic structures, as discussed below.

Now we focus on the magnetotransport properties of  $\text{Fe}_{3-x}\text{GeTe}_2$  crystals to confirm the large AHE experimentally. For  $x \approx 0.1$ , as an example, the magnetization  $M(T)$  for  $H \parallel c(\|z)$  and  $H \parallel a(\|x)$

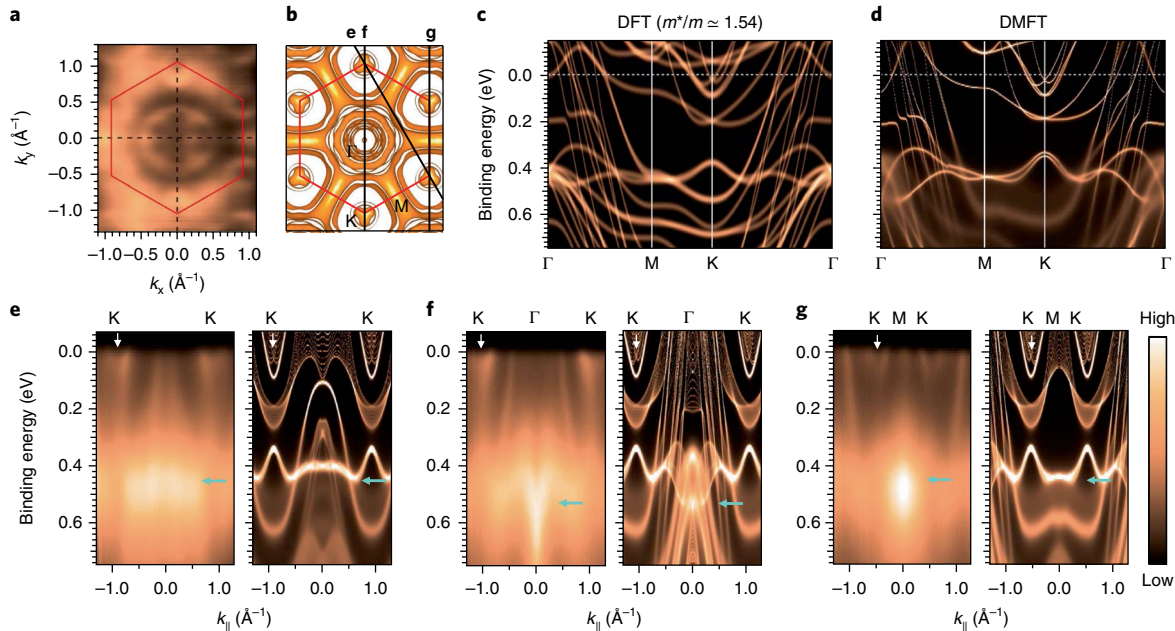


**Fig. 3 | ARPES band mapping compared to DFT and DMFT band calculations for  $\text{Fe}_3\text{x}\text{GeTe}_2$ .** **a**, ARPES intensity at the  $E_F$  in the  $k_x$ - $k_y$  plane—the red hexagon indicates the BZ, which exhibits electron FSs at the K point and hole FSs at the  $\Gamma$  point. The ARPES spectra were taken on a nearly stoichiometric single crystal of  $\text{Fe}_{3-x}\text{GeTe}_2$  ( $x \approx 0.09$ ). **b**, The calculated FS, based on DFT bands, is plotted for the  $\Gamma$  plane, and the black lines indicate the directions of the ARPES cuts presented in **e-g**. **c,d**, The band structure obtained from DFT (**c**) and DMFT (**d**) calculations along the high symmetry lines. The momentum- ( $\mathbf{k}$ ) and energy ( $\omega$ )-dependent spectral function,  $A(\mathbf{k}, \omega)$ , obtained from DMFT calculations is represented very well by the scaling relation of  $E_{\text{DMFT}}(k) = E_{\text{DFT}}(k)/(m^*/m)$  with  $m^*/m \approx 1.54$ , where  $m^*$  and  $m$  are the renormalized and bare band masses, respectively. Although the moderate correlation effects introduce mass renormalization, the crossing point at the K point persists below  $E_F$ . **e**, ARPES spectra along the K-K cut (left) is well reproduced in the  $k_z$ -integrated DMFT spectral function (right). Note that a relatively large  $k_z$  dispersion suppresses the expected spectra from the majority-spin bands near the K point, consistent with experiments. **f,g**, ARPES spectra (left) and  $k_z$ -integrated DMFT spectral function (right) along K- $\Gamma$ -K (**f**) and K-M-K (**g**) cuts match with each other. The electron bands at the K points (yellow arrows) and the bonding states of the  $3d_{z^2-r^2}$  orbital at a binding energy  $E_b \approx 0.4$  eV (cyan arrows) manifest that the electronic structure of  $\text{Fe}_3\text{x}\text{GeTe}_2$  is explained well by DMFT calculations.

(Fig. 4d) and the resistivities  $\rho_{ab}(T)$  and  $\rho_c(T)$  (Fig. 4a) show a clear FM transition at  $T_c = 220$  K. The significant anisotropy in  $M(T)$  reflects the uniaxial magnetocrystalline anisotropy along the  $c$  axis, which is essential to induce the avoided band crossing along the nodal lines and produce a large Berry curvature (Fig. 2e,g). Several FM properties, such as  $T_c$ , the saturated moment  $M_{\text{sat}}$  and the magnetoresistivity vary with the Fe deficiency, consistent with a previous report<sup>22</sup> (Supplementary Note 3). However, the large AHE remains robust for all the crystals. The transverse conductivity, given as  $\sigma_{xy} = \rho_{xy}/(\rho_{xx}^2 + \rho_{xy}^2)$ , exhibits a large jump of  $\Delta\sigma_{xy} \approx 1,000 \mu\Omega\text{cm}$  and is exclusively determined by the anomalous term, that is,  $\sigma_{xy} \approx \sigma_{xy}^A$ , due to the negligible magnetoresistivity of  $\Delta\rho(H)/\rho(0) \leq 3.5\%$  ( $\Delta\rho_{xx}(H) = \rho_{xx}(H) - \rho_{xx}(0)$ ) as shown in Supplementary Fig. 9. The resulting  $\sigma_{xy}^A$  at low temperatures is  $\approx 140$ – $540 \Omega^{-1}\text{cm}^{-1}$ , which is comparable with  $e^2/h a_z \approx 470 \Omega^{-1}\text{cm}^{-1}$  ( $a_z = 8.17 \text{ \AA}$ , the interlayer distance), the value expected for the quantum Hall effect per atomic layer.

Such a large  $\sigma_{xy}^A$  cannot be induced by extrinsic mechanisms such as skew scattering or side jump in  $\text{Fe}_3\text{x}\text{GeTe}_2$ . Recent theoretical studies on AHE<sup>25,26</sup> clarified that the skew-scattering contribution can be comparable with  $e^2/h a_z$  only in the ultraclean limit,  $E_{\text{SO}} \gg \hbar/\tau$  ( $E_{\text{SO}}$ , SOC energy;  $\tau$ , scattering time), whereas the side-jump contribution is much smaller than  $e^2/h a_z$ , by an order of  $E_{\text{SO}}/E_F \approx 10^{-1}$ – $10^{-3}$ . From the measured longitudinal conductivity  $\sigma_{xx} = \rho_{xx}/(\rho_{xx}^2 + \rho_{xy}^2) \approx 10^3 \Omega^{-1}\text{cm}^{-1}$  (Supplementary Figs. 11 and 12) and also the presence of scattering centres seen in scanning tunnelling microscopy (STM) (Supplementary Note 4), we conclude that  $\text{Fe}_{3-x}\text{GeTe}_2$  is in the moderately dirty regime ( $E_{\text{SO}} \approx \hbar/\tau$ ). In this regime, the skew-scattering contribution is much smaller than the Berry curvature

contribution. This conclusion is further supported by the scaling behaviour of  $\sigma_{xy} \propto \sigma_{xx}^\alpha$  with  $\alpha \approx 1.7(1)$  for various Fe-deficient crystals (Supplementary Fig. 12), consistent with the theoretical expectation of  $\alpha = 1.6$  (ref. <sup>25</sup>). Also, we obtained a large  $\sigma_{xy}^A$  of  $\sim 180 \Omega^{-1}\text{cm}^{-1}$  from the DFT calculations due to the intrinsic Berry curvature from the nodal lines, which is in a relatively good agreement with the experimental values. We note that the correlation effect, confirmed by the DFT + DMFT calculations and the ARPES (Fig. 3), should enhance the total Berry curvature and the calculated  $\sigma_{xy}^A$ . This is because the larger portion of the nodal line is expected to be in the resonance condition, taking into account the band renormalization. Also, the minority bands, which are located slightly above  $E_F$  in the DFT calculations and contribute negatively to the Berry curvature, are expected to shift to higher energies, further away from the  $E_F$  (Supplementary Fig. 5). These correlation effects may explain the remaining discrepancy between experiment and calculation, which requires further studies. Nevertheless, our observations strongly suggest that the large Berry curvature from the nodal line is the main source for the observed large  $\sigma_{xy}^A$ .

Finally, we compare the AHE of  $\text{Fe}_3\text{x}\text{GeTe}_2$  with those of other itinerant ferromagnets. Here we employ two characteristic parameters, the anomalous Hall angle,  $\Theta_{\text{AH}}$ , and the anomalous Hall factor,  $S_{\text{H}}$  (ref. <sup>27</sup>).  $\Theta_{\text{AH}}$  is determined by the ratio of  $\sigma_{xy}^A / \sigma_{xx}$ , which measures the relative contribution of the anomalous Hall current with respect to the normal current<sup>26</sup>.  $S_{\text{H}} = \sigma_{xy}^A / M$  estimates the relative magnitude of the anomalous Hall current with respect to the magnetization. Therefore, both  $\Theta_{\text{AH}}$  and  $S_{\text{H}}$  quantify the relative strength of the AHE. For  $\text{Fe}_{3-x}\text{GeTe}_2$  crystals,  $\Theta_{\text{AH}}$  and  $S_{\text{H}}$  are moderately reduced with increasing temperature (Fig. 4c,f) due to inelastic scattering<sup>28</sup>. The maximum values of  $\Theta_{\text{AH}} \approx 0.09$  and  $S_{\text{H}} \approx 0.16 \text{ V}^{-1}$

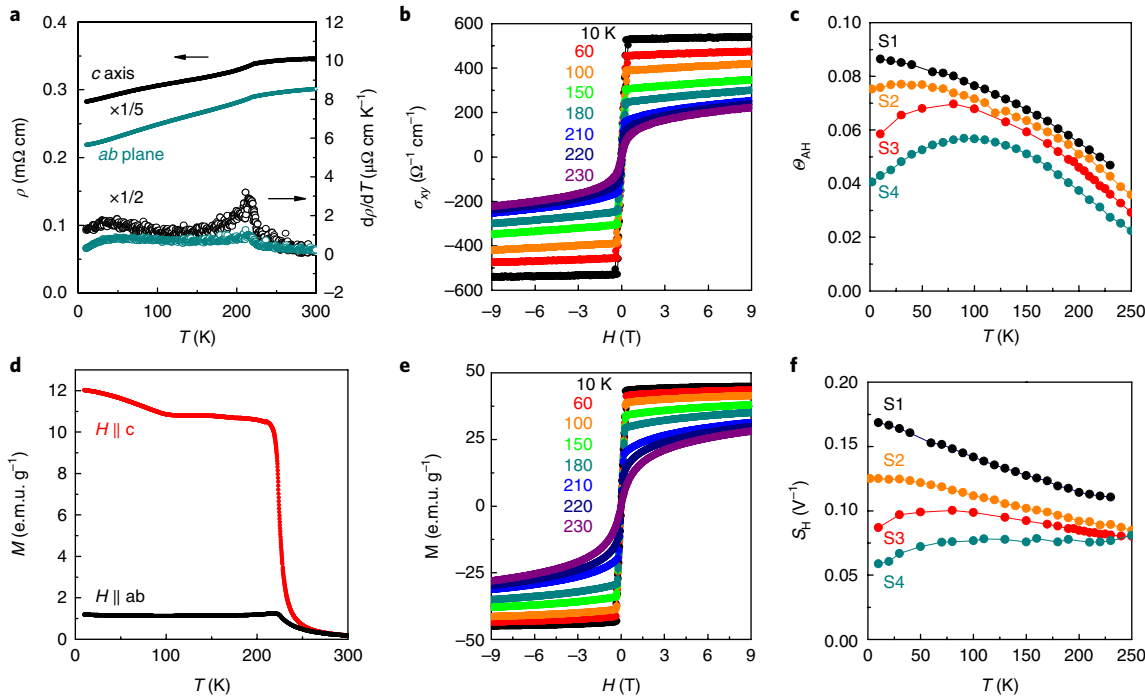


**Fig. 4 | AHE of  $\text{Fe}_3\text{GeTe}_2$  single crystals.** **a**, Temperature dependence of the electrical resistivity  $\rho$  (solid line) and its derivative of resistivity  $d\rho/dT$  (open symbols) with current  $I \parallel c$  and  $I \parallel a$ . The clear kink at  $T_c = 220$  K indicates the ferromagnetic transition. **b**, Magnetic field dependent Hall conductivity  $\sigma_{xy}(H)$  of a single crystal (S1) at various temperatures for  $H \parallel c$ . **c**, Temperature dependence of  $\Theta_{\text{AH}} = \sigma_{xy}^A/\sigma_{xx}$  measured from four  $\text{Fe}_{3-x}\text{GeTe}_2$  single crystals, S1, S2, S3 and S4, with different Fe deficiencies,  $x = 0.09(5), 0.12(5), 0.16(5)$  and  $0.20(6)$ , respectively. **d**, Temperature dependence of the magnetization  $M(T)$  taken at  $H = 1\text{kOe}$ . The anisotropy in  $M(T)$  under  $H \parallel c$  and  $H \parallel ab$  reveals the easy-axis anisotropy along the  $c$  axis. **e**, Magnetic field dependent magnetization  $M(H)$  of S1 at various temperatures for  $H \parallel c$ . **f**, Temperature dependence of  $S_H = \sigma_{xy}^A/M$  for S1-S4. The errors in the experimental data are smaller than the size of the points. e.m.u., electromagnetic unit.

are obtained for the most-conducting crystals at low temperatures, which turn out to be the largest among those of itinerant ferromagnets, as shown in Fig. 5.

Among the itinerant ferromagnets, it is rare to find a system that has both  $\Theta_{\text{AH}}$  and  $S_H$  high at the same time. Even the recently discovered Mn-based antiferromagnets<sup>29</sup> or half-Heusler antiferromagnets<sup>30</sup> have either a significantly enhanced  $S_H$  with a small  $\Theta_{\text{AH}}$  or vice versa. To produce the large anomalous Hall current, that is, a large  $\Theta_{\text{AH}}$  or  $S_H$ , the intrinsic  $\sigma_{xy}^A$  needs to be kept large even with a large scattering or a small  $\sigma_{xx}$ . Near the strongly dirty regime with a small  $\sigma_{xx}$ , however,  $\sigma_{xy}^A$  is suppressed more drastically than  $\sigma_{xx}$ , due to quasiparticle damping or spoiling the resonating condition<sup>25</sup>, whereas  $M$  is less affected<sup>31</sup>. Therefore, the FM systems that have a large  $S_H$  are typically in the moderately dirty regime with a relatively high  $\sigma_{xx}$  and thus exhibit a small  $\Theta_{\text{AH}}$  (Fig. 5). Such a behaviour is also observed in the magnetically doped semiconductors near to the hopping transport regime, as discussed in Supplementary Note 5. In this regard,  $\text{Fe}_{3-x}\text{GeTe}_2$  is exceptional as it has a large  $\Theta_{\text{AH}}$  and  $S_H$  simultaneously, which suggests that the AHE of  $\text{Fe}_3\text{GeTe}_2$  is unusually immune to impurity scattering. This is, in fact, the consequence of the presence of the nodal lines in  $\text{Fe}_3\text{GeTe}_2$ . In other FM metals, 0D monopoles in the momentum space mostly contribute to the total Berry curvature. In this case, the resonance condition has a small energy scale, set by  $E_{\text{SO}}$ , and can easily be spoiled by impurity doping/scattering or even temperature variation<sup>32</sup>. In contrast,  $\text{Fe}_3\text{GeTe}_2$  has 1D nodal lines that disperse along the  $k_z$  direction. Therefore, the resonance condition is satisfied within a relatively large energy window of  $\sim 100$  meV, determined by both  $E_{\text{SO}}$  and the bandwidth along the nodal lines, which keeps the intrinsic  $\sigma_{xy}^A$  robust against large scattering.

Our findings highlight that the orbital-driven nodal line is an effective source of a large AHE in hexagonal vdW ferromagnets. As

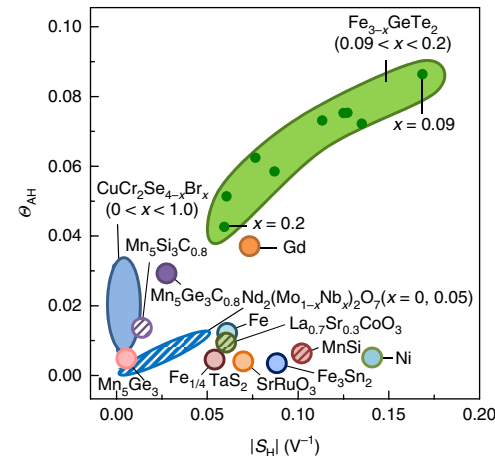


**Fig. 5 | Anomalous Hall angle and anomalous Hall factor of  $\text{Fe}_{3-x}\text{GeTe}_2$  and metallic ferromagnets.** The absolute values of the anomalous Hall angle  $\Theta_{\text{AH}} = \sigma_{xy}^A/\sigma_{xx}$  and the anomalous Hall factor  $S_H = \sigma_{xy}^A/M$  are taken at low temperatures ( $T \ll T_c$ ) from nine  $\text{Fe}_{3-x}\text{GeTe}_2$  single crystals (S1-S9) and various metallic ferromagnets<sup>25-39</sup>. In these metallic ferromagnets, AHE is mainly determined by the Berry curvature in the momentum space near the avoided band crossing due to SOC. The data points for  $\text{Fe}_{3-x}\text{GeTe}_2$  change monotonically as  $x$  varies between the two end points at  $x = 0.09$  and  $x = 0.2$ . Detailed information is given in Supplementary Tables 2 and 3.

the topological nodal line is protected by crystalline symmetries, it can be observed ubiquitously in any system that shares the same symmetry conditions as those in  $\text{Fe}_3\text{GeTe}_2$ , such that: (1) an in-plane trigonal symmetry in the layers, (2) the presence of crystalline

symmetries that connect two layers with the unit cell and (3) 3d bands with finite orbital angular momenta at  $E_F$ . For example, 2H-type transition metal dichalcogenides, typical vdW materials, could be potential candidates when they become FM. Furthermore, as the band crossing is present even in a bilayer, mechanically exfoliated ultrathin crystals offer a promising platform to realize the quantized AHE. Our work thus offers guidelines for the design of FM vdW materials with a large AHE and will stimulate further search for 2D materials with various spin- and orbital-dependent electronic functions.

## Methods

Methods, including statements of data availability and any associated accession codes and references, are available at <https://doi.org/10.1038/s41563-018-0132-3>.

Received: 2 October 2017; Accepted: 13 June 2018;

Published online: 16 July 2018

## References

- Chiu, C. K., Teo, J. C. Y., Schnyder, A. P. & Ryu, S. Classification of topological quantum matter with symmetries. *Rev. Mod. Phys.* **88**, 1–63 (2016).
- Bansil, A., Lin, H. & Das, T. Colloquium: topological band theory. *Rev. Mod. Phys.* **88**, 1–37 (2016).
- Wan, X., Turner, A. M., Vishwanath, A. & Savrasov, S. Y. Topological semimetal and Fermi-arc surface states in the electronic structure of pyrochlore iridates. *Phys. Rev. B* **83**, 205101 (2011).
- Burkov, A. A. & Balents, L. Weyl semimetal in a topological insulator multilayer. *Phys. Rev. Lett.* **107**, 127205 (2011).
- Yang, B.-J. & Nagaosa, N. Classification of stable three-dimensional Dirac semimetals with nontrivial topology. *Nat. Commun.* **5**, 4898 (2014).
- Weng, H., Fang, C., Fang, Z., Bernevig, B. A. & Dai, X. Weyl semimetal phase in noncentrosymmetric transition-metal monophosphides. *Phys. Rev. X* **5**, 011029 (2015).
- Yang, B.-J., Morimoto, T. & Furusaki, A. Topological charges of three dimensional Dirac semimetals with rotation symmetry. *Phys. Rev. B* **92**, 165120 (2015).
- Kim, Y., Wieder, B. J., Kane, C. L. & Rappe, A. M. Dirac line nodes in inversion-symmetric crystals. *Phys. Rev. Lett.* **115**, 036806 (2015).
- Fang, C., Chen, Y., Kee, H. Y. & Fu, L. Topological nodal line semimetals with and without spin-orbital coupling. *Phys. Rev. B* **92**, 081201 (2015).
- Yang, B.-J., Bojesen, T. A., Morimoto, T. & Furusaki, A. Topological semimetals protected by off-centered symmetries in nonsymmorphic crystals. *Phys. Rev. B* **95**, 075135 (2017).
- Fang, C., Weng, H., Dai, X. & Fang, Z. Topological nodal line semimetals. *Chin. Phys. B* **25**, 117106 (2016).
- Liu, Z. K. et al. Discovery of a three-dimensional topological Dirac semimetal,  $\text{Na}_3\text{Bi}$ . *Science* **343**, 864–867 (2014).
- Xu, S.-Y. et al. Discovery of a Weyl fermion semimetal and topological Fermi arcs. *Science* **349**, 613–617 (2015).
- Xiong, J. et al. Evidence for the chiral anomaly in the Dirac semimetal  $\text{Na}_3\text{Bi}$ . *Science* **350**, 413–416 (2015).
- Huang, X. et al. Observation of the chiral-anomaly-induced negative magnetoresistance in 3D Weyl semimetal TaAs. *Phys. Rev. X* **5**, 031023 (2015).
- Shin, D. et al. Violation of Ohm's law in a Weyl metal. *Nat. Mater.* **16**, 1096–1099 (2017).
- Chang, G. et al. Room-temperature magnetic topological Weyl fermion and nodal line semimetal states in half-metallic Heusler  $\text{Co}_2\text{TiX}$  ( $X = \text{Si}, \text{Ge}$ , or  $\text{Sn}$ ). *Sci. Rep.* **6**, 38839 (2016).
- Chang, G. et al. Magnetic and noncentrosymmetric Weyl fermion semimetals in the RAlGe family of compounds ( $R$  = rare earth). *Phys. Rev. B* **97**, 041108(R) (2018).
- Burkov, A. A. Anomalous Hall effect in Weyl metals. *Phys. Rev. Lett.* **113**, 187202 (2014).
- Ueda, K. et al. Anomalous domain-wall conductance in pyrochlore-type  $\text{Nd}_2\text{Ir}_2\text{O}_7$  on the verge of the metal-insulator transition. *Phys. Rev. B* **89**, 075127 (2014).
- Chen, B. et al. Magnetic properties of layered Itinerant electron ferromagnet  $\text{Fe}_3\text{GeTe}_2$ . *J. Phys. Soc. Jpn.* **82**, 124711 (2013).
- May, A. F., Calder, S., Cantoni, C., Cao, H. & McGuire, M. A. Magnetic structure and phase stability of the van der Waals bonded ferromagnet  $\text{Fe}_{3-x}\text{GeTe}_2$ . *Phys. Rev. B* **93**, 014411 (2016).
- Tomczak, J. M., van Schilfgaarde, M. & Kotliar, G. Many-body effects in iron pnictides and chalcogenides: nonlocal versus dynamic origin of effective masses. *Phys. Rev. Lett.* **109**, 237010 (2012).
- Zhu, J.-X. et al. Electronic correlation and magnetism in the ferromagnetic metal  $\text{Fe}_3\text{GeTe}_2$ . *Phys. Rev. B* **93**, 144404 (2016).
- Onoda, S., Sugimoto, N. & Nagaosa, N. Quantum transport theory of anomalous electric, thermoelectric, and thermal Hall effects in ferromagnets. *Phys. Rev. B* **77**, 165103 (2008).
- Nagaosa, N., Sinova, J., Onoda, S., MacDonald, A. H. & Ong, N. P. Anomalous Hall effect. *Rev. Mod. Phys.* **82**, 1539–1592 (2010).
- Lee, M., Onose, Y., Tokura, Y. & Ong, N. P. Hidden constant in the anomalous Hall effect of high-purity magnet MnSi. *Phys. Rev. B* **75**, 172403 (2007).
- Checkelsky, J. G., Lee, M., Morosan, E., Cava, R. J. & Ong, N. P. Anomalous Hall effect and magnetoresistance in the layered ferromagnet  $\text{Fe}_{1/4}\text{TaS}_2$ . *Phys. Rev. B* **77**, 014433 (2008).
- Nakatsuji, S., Kiyohara, N. & Higo, T. Large anomalous Hall effect in a non-collinear antiferromagnet at room temperature. *Nature* **527**, 212–215 (2015).
- Suzuki, T. et al. Large anomalous Hall effect in a half-Heusler antiferromagnet. *Nat. Phys.* **12**, 1119–1123 (2016).
- Sangiao, S. et al. Anomalous Hall effect in  $\text{Fe}(001)$  epitaxial thin films over a wide range in conductivity. *Phys. Rev. B* **79**, 014431 (2009).
- Fang, Z. et al. The anomalous Hall effect and magnetic monopoles in momentum space. *Science* **302**, 92–95 (2003).
- Lee, W.-L., Watauchi, S., Miller, V. L., Cava, R. J. & Ong, N. P. Dissipationless anomalous Hall current in the ferromagnetic spinel  $\text{CuCr}_2\text{Se}_{4-x}\text{Br}_x$ . *Science* **303**, 1647–1649 (2004).
- Surges, C., Fischer, G., Winkel, P. & Lohneysen, H. V. Magnetotransport in ferromagnetic  $\text{Mn}_3\text{Ge}_3$ ,  $\text{Mn}_5\text{Ge}_3\text{C}_{0.8}$ , and  $\text{Mn}_5\text{Si}_3\text{C}_{0.8}$  thin films. *Phys. Rev. B* **90**, 104421 (2014).
- Baily, S. A. & Salamon, M. B. Berry-phase contribution to the anomalous Hall effect in gadolinium. *Phys. Rev. B* **71**, 104407 (2005).
- Iguchi, S., Hanasaki, N. & Tokura, Y. Scaling of anomalous Hall resistivity in  $\text{Nd}_2(\text{Mo}_{1-x}\text{Nb}_x)_2\text{O}_7$  with spin chirality. *Phys. Rev. Lett.* **99**, 077202 (2007).
- Onose, Y. et al. Doping dependence of the anomalous Hall effect in  $\text{La}_{1-x}\text{Sr}_x\text{CoO}_3$ . *Phys. Rev. B* **73**, 174421 (2006).
- Wang, Q., Sun, S., Zhang, X., Pang, F. & Lei, H. Anomalous Hall effect in a ferromagnetic  $\text{Fe}_3\text{Sn}_2$  single crystal with a geometrically frustrated Fe bilayer Kagome lattice. *Phys. Rev. B* **94**, 075135 (2016).
- Jan, J.-P. & Gijsman, H. M. L'effet Hall du fer et du nickel aux basses températures. *Physica* **18**, 339–355 (1952).

## Acknowledgements

The authors thank H. W. Lee, S. Wimmer and M. H. Lee for fruitful discussion. This work was supported by the Institute for Basic Science (IBS) through the Center for Artificial Low Dimensional Electronic Systems (no. IBS-R014-D1), by POSCO through the Green Science programme, and also by the National Research Foundation (NRF) of Korea through the SRC (no. 2011-0030785) and the Max Planck-POSTECH Center for Complex Phase Materials in Korea (MPK) (no. 2016K1A4A4A0192208). B.-J.Y was supported by the Institute for Basic Science (IBS) in Korea (no. IBS-R009-D1), NRF through Basic Science Research Programs (no. 0426-20170012 and no. 0426-20180011) and the POSCO Science Fellowship of POSCO TJ Park Foundation (no. 0426-20180002). K.K. was supported by NRF through Basic Research Programs (no. 2016R1D1A1B02008461 and no. NRF-2017M2A2A6A01071297), KISTI (no. KSC-2015-C3-068) and MPK (no. 2016K1A4A4A0192208). E.L. and C.K. were supported by IBS (no. IBS-R009-D1 and no. IBS-R009-G2). W.K. was supported by NRF (no. 2015-001948) and Y.J.J. was also supported by NRF (no. 2016R1A2B4016656).

## Author contributions

K.K., B.G.J., J.H.S. and B.I.M. performed the band-structure calculations. E.L. and B.-J.Y. did the theoretical analysis. J.S. and J.S.K. conceived the experiments. J.S. and J.M.O. synthesized the samples. J.S., J.M.O., Y.J. and W.K. carried out the transport and the magnetization measurements. K.-T.K., B.S.K. and C.K. performed the ARPES experiments and analysed the results. J.L. and H.W.Y. contributed to the STM measurements and the analysis. K.K., J.S., B.-J.Y. and J.S.K. co-wrote the manuscript. All the authors discussed the results and commented on the paper.

## Competing interests

The authors declare no competing interests.

## Additional information

Supplementary information is available for this paper at <https://doi.org/10.1038/s41563-018-0132-3>.

Reprints and permissions information is available at [www.nature.com/reprints](http://www.nature.com/reprints).

Correspondence and requests for materials should be addressed to B.-J.Y. or J.S.K.

Publisher's note: Springer Nature remains neutral with regard to jurisdictional claims in published maps and institutional affiliations.

## Methods

**Lattice symmetry and orbital Dresselhaus effect along a nodal line.** Let us first consider the symmetry of the AB-stacked bilayer system. The relevant point group is generated by a three-fold rotation about the  $z$  axis,  $C_{3z}$ , a two-fold rotation about the  $y$  axis,  $C_{2y}$ , and inversion  $P$ , which transform the spatial coordinate  $(x, y, z)$  as:

$$\begin{aligned} C_{3z}: (x, y, z) &\rightarrow (x', y', z) \\ C_{2y}: (x, y, z) &\rightarrow (-x, y, -z) \\ P: (x, y, z) &\rightarrow (-x, -y, -z) \end{aligned} \quad (2)$$

where  $x' + iy' = e^{i\frac{2\pi}{3}}(x + iy)$ . At the K point, the system is invariant under  $C_{3z}$ ,  $C_{2y}$  and  $PT$ .

According to the first principles calculation, the wavefunction of the orbital split states near the K point is mainly composed of the  $d$  orbitals of the six Fe atoms ( $\text{Fe}^{(1-6)}$ ) in a unit cell, that is, the  $d_{xz}$  and  $d_{yz}$  orbitals of  $\text{Fe}^{(1,2,3,4)}$  and the  $d_{x^2-y^2}$  and  $d_{xy}$  orbitals of  $\text{Fe}^{(5,6)}$ . Here,  $\text{Fe}^{(1,3)}$  ( $\text{Fe}^{(2,4)}$ ) indicate the two Fe atoms that constitute a dumbbell in the lower (upper) layer and  $\text{Fe}^{(5)}$  ( $\text{Fe}^{(6)}$ ) denotes the atom in the lower (upper) honeycomb plane. These 12  $d$  orbitals, which form a basis for group representations, can be arranged in the following way:

$$\begin{aligned} |L_z = \pm 1\rangle_a &\equiv |\pm 1\rangle_a = \frac{1}{\sqrt{2}}(|d_{xz}\rangle_a \pm i|d_{yz}\rangle_a) \quad (a=1,2,3,4) \\ |L_z = \pm 2\rangle_b &\equiv |\pm 2\rangle_b = \frac{1}{\sqrt{2}}(|d_{x^2-y^2}\rangle_b \pm i|d_{xy}\rangle_b) \quad (b=5,6) \end{aligned} \quad (3)$$

It is straightforward to show how the bases transform under  $C_{3z}$ ,  $C_{2y}$ , and  $P$ . One can choose the location of the rotation axis for  $C_{3z}$  to pass through the  $\text{Fe}^{(1)}-\text{Fe}^{(3)}$  and  $\text{Fe}^{(2)}-\text{Fe}^{(4)}$  dumbbells. In this case, as the  $C_{3z}$  symmetry induces a translation in the position of the  $\text{Fe}^{(5,6)}$  atoms in a honeycomb plane, we need to consider not only the phase change due to the angular momentum of the  $d$  orbital itself, but also the phase due to the wave vector  $\mathbf{k}$  of the Bloch wavefunction given by  $\mathbf{k} \cdot \mathbf{a}$ . The transformation properties of the bases are summarized in Supplementary Table 1.

In particular, along the KH line with the momentum  $\mathbf{k} = (0, \frac{4\pi}{3a}, k_z)$ , the relevant phase change is  $e^{i\mathbf{k} \cdot \mathbf{a}} = e^{i\frac{4\pi}{3}} \equiv e^{i\phi}$ , which cancels the phase change due to  $C_{3z}$  rotation of the states  $| -2 \rangle_5$  and  $| +2 \rangle_6$ , hence,  $| -2 \rangle_5$  and  $| +2 \rangle_6$  transform under  $C_{3z}$  like the states with zero angular momentum, and thus each of them makes a 1D irreducible representation, whereas all the other ten basis states make a 2D irreducible representation that results in a two-fold degenerate band crossing point. More explicitly, one can find that the 12 basis states can be decomposed into  $\Gamma = 1A_1 + 1A_2 + 5E_1$  so that the  $| -2 \rangle_5$  and  $| +2 \rangle_6$  orbitals belong to 1D representations whereas the other ten states form five pairs, each of which forms 2D representations. Similarly, it is straightforward to see that  $| +2 \rangle_5$  and  $| -2 \rangle_6$  constitute 1D representations at the  $K'$  point. Using a pair of states  $\langle |A\rangle, |B\rangle$  to form a basis for a 2D irreducible representation, one can easily find that  $C_{2y}$  and  $C_{3z}$  can be represented as  $C_{2y} = \tau_x$  and  $C_{3z} = \cos\frac{2\pi}{3} + i\sin\frac{2\pi}{3}\tau_z$ , where the Pauli matrices  $\tau_{x,y,z}$  are defined as  $\tau_0 = |A\rangle\langle A| + |B\rangle\langle B|$ ,  $\tau_z = |A\rangle\langle A| - |B\rangle\langle B|$ ,  $\tau_+ = |A\rangle\langle B|$  and  $\tau_- = |B\rangle\langle A|$ .

The effective Hamiltonian can be constructed by considering the following transformation properties:

$$\begin{aligned} C_{3z}: (k_{\pm}, k_z) &\rightarrow \left(e^{\pm i\frac{2\pi}{3}}k_{\pm}, k_z\right), (\tau_{\pm}, \tau_z) \rightarrow \left(e^{\pm i\frac{4\pi}{3}}\tau_{\pm}, \tau_z\right) \\ C_{2y}: (k_{\pm}, k_z) &\rightarrow (-k_{\mp}, -k_z), (\tau_{\pm}, \tau_z) \rightarrow (\tau_{\mp}, -\tau_z) \end{aligned} \quad (4)$$

which leads to the following effective Hamiltonian with the Dresselhaus-type orbital texture:

$$H_0 = c + \frac{1}{2m_{xy}}(k_x^2 + k_y^2) + \frac{1}{2m_z}k_z^2 + \alpha(k_y\tau_x + k_x\tau_y) \quad (5)$$

Note that one can also obtain a Hamiltonian with the Dresselhaus-type orbit splitting by considering  $PT$  instead of  $C_{2y}$ .  $PT$  is represented as  $\tau_x K$ , which has the transformation property:

$$PT: (k_{\pm}, k_z) \rightarrow (k_{\mp}, k_z), (\tau_{\pm}, \tau_z) \rightarrow (\tau_{\mp}, -\tau_z) \quad (6)$$

and so, using  $C_{3z}$  and  $PT$ , one can obtain:

$$H_0 = c + \frac{1}{2m_{xy}}(k_x^2 + k_y^2) + \frac{1}{2m_z}k_z^2 + \alpha(k_y\tau_x + k_x\tau_y) + \beta(k_x\tau_x - k_y\tau_y) \quad (7)$$

Imposing  $C_{2y}$  additionally makes  $\beta = 0$ .

A similar idea can be used to describe the nodal line along the KH direction in the bulk system. The relevant space group is  $P6_3/mmc$  (No. 194), which is generated by a six-fold screw rotation  $\tilde{C}_{6z}$  together with  $C_{2y}$  and  $P$ , which transform the spatial coordinate  $(x, y, z)$  as:

$$\begin{aligned} \tilde{C}_{6z}: (x, y, z) &\rightarrow \left(x'', y'', z + \frac{1}{2}\right) \\ C_{2y}: (x, y, z) &\rightarrow (-x, y, -z) \\ P: (x, y, z) &\rightarrow (-x, -y, -z) \end{aligned} \quad (8)$$

where  $x'' + iy'' = e^{i\frac{\pi}{3}}(x + iy)$ . At a momentum on the KH line, the system is invariant under  $C_{3z} \equiv [\tilde{C}_{6z}]^2$ ,  $PT$  and  $\tilde{C}_{6z}PC_{2y} \equiv \tilde{C}_{6z}M_y$ , under which the spatial coordinate transforms as:

$$\begin{aligned} C_{3z}: (x, y, z) &\rightarrow (x', y', z + 1) \\ PT: (x, y, z) &\rightarrow (-x, -y, -z)K \\ \tilde{C}_{6z}M_y: (x, y, z) &\rightarrow \left(x'', -y'', z + \frac{1}{2}\right) \end{aligned} \quad (9)$$

where  $K$  denotes the complex conjugation associated with the time-reversal  $T$ . As the system is not invariant under  $C_{2y}$  when  $k_z \neq 0$ , one needs to consider  $\tilde{C}_{6z}M_y$  that also interchanges the orbitals in different layers, like  $C_{2y}$ . It is straightforward to show that the combination of  $C_{3z}$ ,  $PT$  and  $\tilde{C}_{6z}M_y$  leads to the same effective  $2 \times 2$  Hamiltonian with the Dresselhaus-type band splitting as shown above.

**Influence of SOC.** SOC is generally described by the Hamiltonian  $H_{SO} = \sum_i \lambda_{SO} \mathbf{L}_i \cdot \mathbf{S}_i$ , where  $i$  indicates an atomic site. Considering the double degeneracy along the KH line,  $H_{SO}$  can be treated by applying degenerate perturbation theory. The first order energy correction  $E_n^{(1)}$  is obtained by diagonalizing a  $2 \times 2$  matrix with the matrix elements  $\langle \phi_{n,i}^0 | \lambda_{SO} \mathbf{L} \cdot \mathbf{S} | \phi_{n,j}^0 \rangle$ , where  $|\phi_{n,i}^0\rangle$  indicates the degenerate states at the band crossing point. In a ferromagnet with  $\langle \mathbf{S} \rangle \equiv S \neq 0$ , the matrix element can be rewritten as  $\lambda_{SO} S \langle \phi_{n,i}^0 | \mathbf{L} \cdot \hat{\mathbf{n}} | \phi_{n,j}^0 \rangle$  because all states are eigenstates of a designated spin component  $\mathbf{S} \cdot \hat{\mathbf{n}}$ . In the 2D manifold spanned by  $\{|A\rangle, |B\rangle\}$  defined above, one can show that:

$$\langle A | \hat{L}_z | A \rangle = -\langle B | \hat{L}_z | B \rangle = \frac{4}{3}, \langle A | \hat{L}_z | B \rangle = \langle B | \hat{L}_z | A \rangle = 0 \quad (10)$$

thus  $\hat{L}_z = \frac{4}{3}(\langle A | A \rangle - \langle B | B \rangle) = \frac{4}{3}\tau_z$ . Repeating similar calculations, it is straightforward to show that  $\langle \hat{L}_z \rangle = \langle \hat{L}_y \rangle = 0$ . Thus, when the FM moment is along the  $z$  direction,  $H_{SO} \approx \Delta_z \tau_z$  where  $\Delta_z \propto \langle \mathbf{S} \cdot \hat{\mathbf{z}} \rangle$ . Then the full Hamiltonian becomes:

$$H_0 + H_{SO} = c + \frac{1}{2m_{xy}}(k_x^2 + k_y^2) + \frac{1}{2m_z}k_z^2 + \alpha(k_y\tau_x + k_x\tau_y) + \Delta_z \tau_z \quad (11)$$

where one can easily find the gap opening at the degeneracy point, which can generate AHE.

However, as the first-order correction vanishes when the direction of the FM moment is in-plane (that is,  $\hat{\mathbf{n}} \perp \hat{\mathbf{z}}$ ), one should consider higher-order corrections. For instance, the second order correction is:

$$E_{n,ij}^{(2)} = (\lambda_{SO} S)^2 \sum_{n \neq k}^{\infty} \frac{\langle \phi_{n,i}^0 | \mathbf{L} \cdot \hat{\mathbf{n}} | \phi_k^0 \rangle \langle \phi_k^0 | \mathbf{L} \cdot \hat{\mathbf{n}} | \phi_{n,j}^0 \rangle}{E_n^{(0)} - E_n^{(k)}} \quad (12)$$

However, given that only 12 orbitals  $|\pm 1\rangle_{1-4}$  and  $|\pm 2\rangle_{5,6}$  have a dominant contribution to the states near the  $E_p$ , one can show that  $\langle \phi_{n,i}^0 | \mathbf{L} \cdot \hat{\mathbf{n}} | \phi_k^0 \rangle$  vanishes (that is,  $E_n^{(2)} = 0$ ). This is because  $\mathbf{L} \cdot \hat{\mathbf{n}}$  is a linear combination of ladder operators  $L_+$  and  $L_-$  that raises or lowers the angular momentum of the orbital states by  $\pm 1$ , and thus the bases we consider cannot make a non-zero contribution. For the same reason, the effect of SOC vanishes in all orders of the perturbation theory if we only take into account the manifold spanned by the 12 orbitals. Therefore, when the spin is aligned in the in-plane direction, the degeneracy along the nodal line is perturbatively stable in the presence of the SOC, and thus the system remains gapless.

**First principles calculations.** Electronic structure calculations within the DFT were performed by using the full-potential linearized augmented plane wave code WIEN2k<sup>40</sup> and the full-potential local-orbital minimum-basis code FPLO<sup>41</sup>. A spin-orbit interaction term is included in the second-order perturbation manner in Wien2k, whereas in FPLO, full relativistic effects are included in a four-component spinor basis. To calculate the Berry curvature and anomalous Hall coefficients to a high precision, maximally localized Wannier functions are used utilizing Wannier90 code<sup>42</sup>. For the DFT + DMFT calculations, a combination of DFT and DMFT<sup>43</sup>, the DFT calculation are performed with WIEN2K code<sup>40</sup> using a full-potential augmented plane-wave method and the Perdew-Burke-Ernzerhof generalized gradient approximation for the exchange correlation functional<sup>44</sup>. The correlation effect of the  $F$   $d$  orbitals is treated by a DMFT loop on the top of an effective one-electron Hamiltonian generated from the WIEN2k calculation. The quantum impurity model is solved by using a continuous-time quantum Monte Carlo (CTQMC) impurity solver<sup>45</sup>. We perform the calculation with a Coulomb

interaction of  $U=5.0\text{ eV}$  and Hund coupling of  $J=0.9\text{ eV}$  at a temperature  $290\text{ K}$  ( $\beta=40$ ).

**Single-crystal growth and physical property measurements.** Single crystals of  $\text{Fe}_{3-x}\text{GeTe}_2$  were grown by a chemical vapour transport method with iodine as the transport agent. The as-grown single crystals are in a plate shape with a typical size of  $\sim 2 \times 1 \times 0.1\text{ mm}^3$ . X-ray diffraction and energy dispersive spectroscopy confirmed the high crystallinity and slightly Fe-deficient stoichiometry, consistent with a previous report<sup>22</sup>. The magnetic properties were measured along the  $c$  axis or the  $ab$  plane using a superconducting quantum interference device magnetometer (MPMS, Quantum Design). The in-plane resistivity and the Hall coefficient were measured using the standard six-probe method in a Physical Property Measurement System (PPMS-14T, Quantum Design).

**ARPES.** ARPES measurements were performed on the MERLIN beamline (BL 4.0.3) of the Advanced Light Source. The single crystals were cleaved in situ at  $25\text{ K}$  and the vacuum pressure was better than  $5 \times 10^{-11}\text{ torr}$ . The ARPES spectra were collected by using a VG-SCIENTA R8000 electron analyser and the energy resolution was better than  $20\text{ meV}$  at a photon energy of  $h\nu=90\text{ eV}$ .

**Data availability.** The data that support the findings of this study are available from the corresponding authors on request.

## References

40. Blaha, P., Schwarz, K., Madsen, G. K. H., Kvasnicka, D. & Luitz, J. WIEN2k, *An Augmented Plane Wave Plus Local Orbitals Program for Calculating Crystal Properties* (Technical University of Wien, 2001).
41. Koepernik, K. & Eschrig, H. Full-potential nonorthogonal local-orbital minimum-basis band-structure scheme. *Phys. Rev. B* **75**, 1743 (1999).
42. Mostofi, A. A. et al. An updated version of Wannier90: a tool for obtaining maximally-localised Wannier functions. *Comput. Phys. Commun.* **185**, 2309–2310 (2014).
43. Haule, K., Yee, C. H. & Kim, K. Dynamical mean-field theory within the full-potential methods: Electronic structure of  $\text{CeIrIn}_5$ ,  $\text{CeCoIn}_5$ , and  $\text{CeRhIn}_5$ . *Phys. Rev. B* **81**, 195107 (2010).
44. Perdew, J. P., Burke, K. & Ernzerhof, M. Generalized gradient approximation made simple. *Phys. Rev. Lett.* **77**, 3865–3868 (1996).
45. Haule, K. Quantum Monte Carlo impurity solver for cluster dynamical mean-field theory and electronic structure calculations with adjustable cluster base. *Phys. Rev. B* **75**, 155113 (2007).